A Small-Scale Dynamic Model Using a Terrain-Following Coordinate Transformation

TERRY L. CLARK

Atmospheric Environment Service, Downsview, Ontario M3H 5T4, Canada

This paper describes a three-dimensional finite-difference model of air flow over an irregular lower surface. The model is nonhydrostatic and the anelastic approximation has been used to filter sound waves. Second-order difference equations are employed which provide excellent momentum and energy budgets. An outflow radiation boundary condition using a generalized Kreiss extrapolation scheme has been designed and implemented.

Some two-dimensional applications of the model to air flow over a "Witch of Agnesi" mountain barrier are described. Comparison with the linear theory of Queney indicates, for the cases treated, that the nonlinearity of the boundary condition has a first-order effect on the resulting flow.

1. INTRODUCTION

There are a wide variety of problems of interest to both fluid dynamicists and meteorologists which require a limited-area model of the equations of fluid flow and thermodynamics on a small spatial scale where the lower boundary of the model is an irregular surface. Problems of this type include the modeling of air flow over an urban region and the associated dispersion and advection of pollutants, convective scale dynamics in mountainous regions, mountain wave drag studies, and possibly even boundary layer parameterization studies where the nonhydrostatic dynamics require explicit treatment. It is well known in atmospheric dynamics that the scale analysis leading to the hydrostatic approximation for tropospheric motions breaks down when the resolvable horizontal and vertical scales are the same order. Problems of this nature require the treatment of nonhydrostatic dynamics and this is often accomplished by invoking the "anelastic" approximation [1–3] in which sound waves are filtered by appropriate modification of the mass continuity equation.

The purpose of this paper is to describe a three-dimensional, limited-area, anelastic finite-difference model in which the equations of motion and the first law of thermodynamics are solved in a domain which has an irregular lower boundary. Some results from a two-dimensional application of the model to the problem of flow over a "bell-shaped" ridge are presented for ridge heights of 100 m and 1 km, where in both cases the half-width of the ridge is 3 km. The first case can be considered as one for which the lower boundary condition might be expected to approximate that employed in linear theory, whereas in the second case one expects a significant contribution to

186

the near-surface flow from the nonlinearity of the boundary condition. The linearity of the boundary condition is based upon both the aspect ratio of the ridge and its cross-sectional area. The two calculations presented in this paper consider aspect ratios (height/half-width) of 1/30 and 1/3 where the mountain half-width was kept constant at 3 km. The first case has a small enough aspect ratio that one would expect linear theory [4, 5] to provide a reasonably accurate approximation. The model calculations described here will be compared with a linear calculation of Peltier [18] and the departures from linear theory will be discussed for the above two cases.

The work of Gal-Chen and Sommerville [6, 7] demonstrated the feasibility of using the terrain-following coordinate transformation

$$\bar{z} = H(z - z_s)/(H - z_s)$$

for the treatment of small-scale dynamics. In this transformation $z_s(x, y)$ is the topographic field height and H is the domain height of the model. A review of other approaches which have been employed to treat the irregular lower boundary is given in [6]. This coordinate transformation will be adopted in the present paper although the numerical methods employed to solve the transformed equation as well as the form of the equations themselves are quite different from those of [6, 7]. The Chorin [8] time-differencing scheme used in [7] has been replaced by centered time differencing. The emphasis in the construction of the present model is on matching the conservative aspects of the time- and spatial-differencing schemes. As will be shown in the numerical analysis and results there is one main nonphysical (numerical) kinetic energy source–sink term (which is relatively insensitive to time resolution) due to pressure truncation errors and this is about three orders of magnitude below the main physical source–sink terms. The use of centered time differencing also keeps the effect of the nonlinear advective terms on the kinetic energy well below this level.

The equations are cast in flux form (e.g., [23, 24]), where the Cartesian velocity components (u, v, w) are explicitly employed in forming the x, y, and z momentum equations, respectively. This differs from the approach taken in [7], where an ω tendency was calculated explicitly with ω the velocity normal to the $\bar{z} = $ constant surfaces. This resulted in the appearance of Christoffel symbols of the second kind in the ω equation as part of the advection terms. These terms are of a nonconservative nature and make it very difficult to allow for the conservation of either momentum or kinetic energy in the model. Thus, one improvement of this model over that of [7] is the fully conservative formulation of all advection terms for the momentum and kinetic energies in the x, y, and z directions. The principles deduced by Arakawa [9] were used to keep the advective terms conservative.

Some of the model's practical aspects discussed in this paper are the techniques employed for the solution of the diagnostic pressure equation; the suppression of wave reflections off the upper lid through the use of Rayleigh friction; and the design of a generalized Kreiss [15] radiation boundary condition at the outflow boundary, which proved very efficient for the calculations presented in this paper.

Following a suggestion by Orlanski [16] a time-and height-dependent phase velocity

was employed to generalize the Kreiss [15] method for the outflow boundary. This was found to result in only insignificant reflections from this region. Orlanski [10] has developed a radiation condition which uses the Sommerfeld condition to calculate the phase velocity representative of conditions just upstream of the boundary and an extrapolation scheme to calculate variables at the boundary. His method was not available at the time this work was completed so that the methods used in the present context are somewhat different. Hopefully they will add something useful to the growing literature on this important problem.

2. ANALYTICAL EQUATIONS OF THE MODEL

2.a. *Equations in Cartesion Coordinates*

The momentum equations are given by

$$\bar{\rho}\,\frac{du}{dt} - \bar{\rho}vf = -\frac{\partial p'}{\partial x} + \frac{\partial}{\partial x}\,\tau_{11} + \frac{\partial}{\partial y}\,\tau_{12} + \frac{\partial}{\partial z}\,\tau_{13} - \bar{\rho}u'/\tau_{R}\,, \tag{2.1}$$

$$\bar{\rho}\,\frac{dv}{dt} + \bar{\rho}uf = -\frac{\partial p'}{\partial y} + \frac{\partial}{\partial x}\,\tau_{21} + \frac{\partial}{\partial y}\,\tau_{22} + \frac{\partial}{\partial z}\,\tau_{23} - \bar{\rho}v'/\tau_{R}\,, \tag{2.2}$$

$$\bar{\rho}\,\frac{dw}{dt} = -\frac{\partial p'}{\partial z} - \rho'g + \frac{\partial}{\partial x}\,\tau_{31} + \frac{\partial}{\partial y}\,\tau_{32} + \frac{\partial}{\partial z}\,\tau_{33} - \bar{\rho}w/\tau_{R}\,, \tag{2.3}$$

and the "anelastic" form of the mass continuity equation as

$$\frac{\partial}{\partial x}\,(\bar{\rho}u) + \frac{\partial}{\partial y}\,(\bar{\rho}v) + \frac{\partial}{\partial z}\,(\bar{\rho}w) = 0. \tag{2.4}$$

Map factors are not included in the model as it is intended for use in the study of small-scale phenomena. The terms u, v, and w are the fluid velocity components in the x, y, and z directions, respectively; τ_{ij} is the Reynolds stress tensor which will be parameterized, using a first-order theory, in such a way as to represent subgrid scale turbulence. The last terms on the right-hand sides of (2.1) to (2.3) are Rayleigh friction terms which are included for purely numerical reasons. The integration domain is bounded above by a rigid lid which has the effect of reflecting vertically propagating waves. In order to suppress upper-lid reflections the Rayleigh friction time constant, τ_{R}, is allowed to have finite values in the upper levels. Below some level (five grid levels for the present calculations) τ_{R} is set equal to infinity. Thus the model solutions in the Rayleigh friction regions are rather unphysical and will not be used in the detailed analysis of the fluid flow. Terms u' and v' are some appropriate deviations of u and v from a mean value. The thermodynamic variables are separated into two components, the terms with overbars denote a basic state of the environment which

is in hydrostatic balance, and the primed variables denote perturbations from the basic state. The thermodynamic variables may then be expanded as

$$
\begin{aligned}
\rho &= \bar{\rho}(z) + \rho'(\mathbf{x}, t), \\
p &= \bar{p}(z) + p'(\mathbf{x}, t), \\
\theta &= \bar{\theta}(z) + \theta'(\mathbf{x}, t), \\
T &= \overline{T}(z) + T'(\mathbf{x}, t),
\end{aligned}
\tag{2.5}
$$

where ρ, p, θ, and T are the dry air density, pressure, potential temperature, and temperature, respectively.

As shown in [1–3] all frequencies avove the Brunt–Väisälä frequency are filtered when the local time rate of change of ρ is dropped from the mass continuity equation. Similar to the Boussinesq [11] equations, the present set ignores variations of density from the background profile except where they are multiplied by the acceleration of gravity, g. The deep equations of Ogura and Phillips [3] have been employed in the present calculations and since these presume the base state to be isentropic, the base-state thermodynamic variables have the forms

$$
\bar{\theta}(z) = \Theta,
\tag{2.6}
$$

$$
\overline{T}(z) = \Theta(1 - z/H_s),
\tag{2.7}
$$

$$
\bar{p}(z) = P_0(1 - z/H_s)^{1/\kappa},
\tag{2.8}
$$

$$
\bar{\rho}(z) = P_0(1 - z/H_s)^{1/\kappa - 1}/(R_d\Theta),
\tag{2.9}
$$

where P_0 is the surface pressure at $z = 0$, $\kappa = R_d/C_p$, and H_s $(= C_p\Theta/g)$ is the isentropic scale height. In deriving (2.6) to (2.9) the ideal gas law

$$
p = \rho R_d T,
\tag{2.10}
$$

the definition of potential temperature

$$
\theta = T(p/P_0)^{-\kappa},
\tag{2.11}
$$

and the hydrostatic balance relation

$$
dp/dz = -\rho g
\tag{2.12}
$$

were applied to the reference state variables. A linearization of (2.10) and (2.11) results in

$$
\rho' = (p'/C^2) - \bar{\rho}(\theta'/\Theta),
\tag{2.13}
$$

where C^2 $(= \gamma R_d \overline{T})$ is the square of the adiabatic sound speed. The numerical model is coded in such a manner as to make it an easy matter to change from the present perturbation equations to a possibly more accurate set in the future. We could, for example, elect to expand the field variables about a given vertical temperature profile. The advantage of the deep equations of Ogura and Phillips is that they have a very simple energy closure against which the model can be easily checked.

The first law of thermodynamics is represented by

$$\bar{\rho}\frac{d\theta}{dt} = \frac{\partial}{\partial x}H_1 + \frac{\partial}{\partial y}H_2 + \frac{\partial}{\partial z}H_3,\qquad(2.14)$$

where the H_i terms represent the turbulent heat flux on the subgrid scale.

The symmetric Reynolds stress tensor is specified in terms of the resolved fields according to a formulation suggested by Smagorinsky [12] and later discussed by Lilly [13] such that

$$\tau_{ij} = \bar{\rho}K_M D_{ij}.\qquad(2.15)$$

The deformation tensor, D_{ij}, is given as

$$D_{ij} = \left(\frac{\partial u_i}{\partial x_j} + \frac{\partial u_j}{\partial x_i} - \frac{2}{3}\delta_{ij}\frac{\partial u_h}{\partial x_h}\right)\qquad(2.16)$$

and the eddy mixing coefficient for momentum as

$$K_M = (k\varDelta)^2 \,|\, \text{Def}\,|,\qquad(2.17)$$

where $\varDelta$ is a measure of the grid resolution of the model and Def is the total deformation calculated with this grid resolution. A value of $k = 0.25$ was used in (2.17). The deformation is given as

$$\text{Def}^2 = \tfrac{1}{2}(D_{11}^2 + D_{22}^2 + D_{33}^2) + D_{12}^2 + D_{13}^2 + D_{23}^2.\qquad(2.18)$$

The turbulent heat flux terms are specified as

$$H_i = \bar{\rho}K_H(\partial\theta/\partial x_i),\qquad(2.19)$$

where $K_H = K_M$ will be assumed. This nonlinear formulation for K_M is reasonable for three-dimensional isotropic subgrid scale turbulence. It is also assumed in (2.17) that there is an instantaneous adjustment of subgrid scale eddies to the mean flow as well as zero turbulent heat flow. More sophisticated first-order subgrid scale formulations for the turbulent mixing terms can be considered which do not assume zero heat flow. These concepts are discussed by Lilly [13].

Equations (2.1) to (2.4) and (2.13) to (2.19) constitute 11 equations for the 11 field variables u, v, w, τ_{ij}, H_i, D_{ij}, Def, K_M, p', ρ', and θ'. The specification of boundary and initial conditions will complete the model description. Both of these latter aspects of the model will be discussed following the presentation of the numerical approximations of the equations.

2b. Coordinate Transformation for Nonvanishing Topography

The model equations are transformed from (x, y, z) to $(x, y, \bar{z})$ coordinates, where

$$\bar{z} = H(z - z_s)/(H - z_s),\qquad(2.20)$$

with $z_s(x, y)$, H the lower and upper boundaries of the integration domain. Following [6] we obtain the Jacobian of the transformation as

$$G^{1/2} = 1 - z_s/H \tag{2.21}$$

and the two metric tensor coefficients as

$$G^{1/2}G^{13} = ((\bar{z}/H) - 1)(\partial z_s/\partial x) \tag{2.22}$$

and

$$G^{1/2}G^{23} = ((\bar{z}/H) - 1)(\partial z_s/\partial y). \tag{2.23}$$

Applying the chain rule, the following relations are obtained.

$$G^{1/2}\frac{\partial \phi}{\partial x}\bigg|_{z=\text{const}} = \frac{\partial}{\partial x}(G^{1/2}\phi)\bigg|_{\bar{z}=\text{const}} + \frac{\partial}{\partial \bar{z}}(G^{1/2}G^{13}\phi), \tag{2.24}$$

$$G^{1/2}\frac{\partial}{\partial y}\phi\bigg|_{z=\text{const}} = \frac{\partial}{\partial y}(G^{1/2}\phi)\bigg|_{\bar{z}=\text{const}} + \frac{\partial}{\partial \bar{z}}(G^{1/2}G^{23}\phi), \tag{2.25}$$

$$G^{1/2}\frac{\partial}{\partial z}\phi = \frac{\partial}{\partial \bar{z}}\phi, \tag{2.26}$$

where ϕ is an arbitrary field variable. Equations (2.24) to (2.26) plus the definition

$$\omega = d\bar{z}/dt = (1/G^{1/2})(w + G^{1/2}G^{13}u + G^{1/2}G^{23}v) \tag{2.27}$$

are used to transform (2.1) to (2.3) to the $(x, y, \bar{z})$ domain.

In the following sections all base-state overbars on the thermodynamic variables will be dropped because they could be confused with some of the numerical operators. The final analytical model equations will not be derived in this paper but will simply be presented in their respective numerical forms. All of the analytical equations and associated terms are easily derived from (2.1) to (2.19) using relations (2.24) to (2.26). It is convenient to Jacobian weight the air density so that in subsequent sections

$$\rho \to G^{1/2}\rho. \tag{2.28}$$

3. NUMERICAL FORM OF THE MODEL EQUATIONS

3a. Basic Numerical Definitions

The staggered grid of Harlow and Welch [14] is employed to represent the fields in finite-difference space. Defining

$$\begin{aligned} x &= (i - \tfrac{3}{2})\,\Delta x && \text{for} \quad i = 1, 2,..., NX, \\ y &= (j - \tfrac{3}{2})\,\Delta y && \text{for} \quad j = 1, 2,..., NY, \\ \bar{z} &= (k - \tfrac{3}{2})\,\Delta z && \text{for} \quad k = 1, 2,..., NZ \end{aligned} \tag{3.1}$$

as the grid center values of $(x, y, \bar{z})$, where Δx, Δy, and Δz are the respective constant grid increments, we have

$$u \equiv u(i \pm \tfrac{1}{2}, j, k),$$
$$v \equiv v(i, j \pm \tfrac{1}{2}, k), \tag{3.2}$$
$$w, \omega \equiv w, \omega(i, j, k \pm \tfrac{1}{2}),$$

and

$$\phi = \phi(i, j, k), \tag{3.3}$$

where ϕ represents any of the scalars ρ, T, θ, p, K_H, Def, τ_{11}, τ_{22}, τ_{33}. The grid locations of the remaining variables are

$$\tau_{12} = \tau_{12}(i \pm \tfrac{1}{2}, j \pm \tfrac{1}{2}, k),$$
$$\tau_{13} = \tau_{13}(i \pm \tfrac{1}{2}, j, k \pm \tfrac{1}{2}), \tag{3.4}$$
$$\tau_{23} = \tau_{23}(i, j \pm \tfrac{1}{2}, k \pm \tfrac{1}{2}),$$

and

$$H_1 = H_1(i \pm \tfrac{1}{2}, j, k),$$
$$H_2 = H_2(i, j \pm \tfrac{1}{2}, k), \tag{3.5}$$
$$H_3 = H_3(i, j, k \pm \tfrac{1}{2}),$$

and

$$\bar{z} = \bar{z}(k \pm \tfrac{1}{2}), \tag{3.6}$$

$$z_s = z_s(i, j). \tag{3.7}$$

The $\tfrac{3}{2}$ enters in (3.1) because the first and last grid points lie outside the integration domain; i.e., explicit treatment of boundary conditions was chosen over implicit treatment.

Shuman-type operators [21] will be used to describe the numerical equations compactly. For an arbitrary dependent variable ϕ and an independent variable η we have

$$\bar{\phi}^\eta = [\phi(\eta + \Delta\eta/2) + \phi(\eta - \Delta\eta/2)]/2, \tag{3.8}$$

$$\delta_\eta \phi = [\phi(\eta + \Delta\eta/2) - \phi(\eta - \Delta\eta/2)]/\Delta\eta, \tag{3.9}$$

where η could be any of x, y, $\bar{z}$, or τ. The time level is given as $t = \tau \, \Delta t$.

3.b. *Numerical Formulation of the Equations*

The momentum equations are given by

$$\delta_t \overline{(\bar{\rho}^x u)}^t + \mathrm{ADVX}^\tau - \overline{(\bar{\rho}^y v}^{xy} f)^\tau = \mathrm{PFX}^\tau + \mathrm{KFX}^{\tau-1} + \mathrm{RAYX}^\tau, \tag{3.10}$$

$$\delta_t \overline{(\bar{\rho}^y v)}^t + \mathrm{ADVY}^\tau + \overline{(\bar{\rho}^x u}^{xy} f)^\tau = \mathrm{PFY}^\tau + \mathrm{KFY}^{\tau-1} + \mathrm{RAYY}^\tau, \tag{3.11}$$

$$\delta_t \overline{(\bar{\rho}^z w)}^t + \mathrm{ADVZ}^\tau = \mathrm{PFZ}^\tau + \mathrm{BY}^\tau + \mathrm{KFZ}^{\tau-1} + \mathrm{RAYZ}^\tau, \tag{3.12}$$

where (3.10) to (3.12) represent the approximation equations for the x, y, and z momentum equations, respectively. The nonlinear advective terms are denoted as ADVX(Y, Z); the Coriolis terms are explicitly given; the pressure gradient terms are denoted as PFX(Y, Z); the eddy mixing terms are denoted as KFX(Y, Z); and the Rayleigh friction terms are denoted as RAYX(Y, Z). All terms are represented using centered time differences except for the diffusion terms, which are represented using forward time steps. The mass continuity equation takes on the simple form

$$\delta_x(\bar{\rho}^x u) + \delta_y(\bar{\rho}^y v) + \delta_z(\bar{\rho}^z \omega) = 0 \tag{3.13}$$

and the first law of thermodynamics is given as

$$\delta_t \overline{(\rho\theta)}^t + \text{ADVT}^\tau = \text{KFT}^{\tau-1}. \tag{3.14}$$

The numerical approximation of the diagnostic equation (2.27) defining the ω field was taken as

$$G^{1/2}\bar{\rho}^z \omega = \bar{\rho}^z w + \overline{G^{1/2}G^{13}\bar{\rho}^x u}^x + \overline{G^{1/2}G^{23}\widetilde{\bar{\rho}^y v}}^y , \tag{3.15}$$

which can be employed to define a transformation operation, $\text{OP}_{\tilde{z}}$, such that

$$G^{1/2}\bar{\rho}^z \omega = \text{OP}_{\tilde{z}}(\bar{\rho}^z w, \bar{\rho}^x u, \bar{\rho}^y v) \tag{3.16}$$

and similarly the inverse operator

$$\bar{\rho}^z w = \text{OP}_z(G^{1/2}\bar{\rho}^z \omega, \bar{\rho}^x u, \bar{\rho}^y v) = \text{OP}_{\tilde{z}}(G^{1/2}\bar{\rho}^z \omega, -\bar{\rho}^x u, -\bar{\rho}^y v). \tag{3.17}$$

The numerical form of $\text{OP}_{\tilde{z}}$ is extremely imortant for the achievement of good vertical moment as well as kinetic energy budgets.

The advective terms conserve the first moments (momentum, potential temperature) under all conditions and conserve the second moments (kinetic energy, potential temperature variance) providing the second time derivatives are negligible. The numerical expressions for the advective terms for momentum are

$$\text{ADVX} = \delta_x(\overline{\bar{\rho}^x u}\,\overline{u}^{x-x}) + \delta_y(\overline{\bar{\rho}^y v}\,\overline{u}^{x-y}) + \delta_z(\overline{\bar{\rho}^z \omega}\,\overline{u}^{x-z}), \tag{3.18}$$

$$\text{ADVY} = \delta_x(\overline{\bar{\rho}^x u}\,\overline{v}^{y-x}) + \delta_y(\overline{\bar{\rho}^y v}\,\overline{v}^{y-y}) + \delta_z(\overline{\bar{\rho}^z \omega}\,\overline{v}^{y-z}), \tag{3.19}$$

$$\text{ADVZ} = \delta_x(\overline{\bar{\rho}^x u}\,\overline{w}^{z-x}) + \delta_y(\overline{\bar{\rho}^y v}\,\overline{w}^{z-y}) + \delta_z(\overline{\bar{\rho}^z \omega}\,\overline{w}^{z-z}), \tag{3.20}$$

and for the potential temperature

$$\text{ADVT} = \delta_x(\bar{\rho}^x u \bar{\theta}^x) + \delta_y(\bar{\rho}^y v \bar{\theta}^y) + \delta_z(\bar{\rho}^z \omega \bar{\theta}^z). \tag{3.21}$$

The numerical form of the pressure gradient terms is

$$\text{PFX} = -\delta_x(G^{1/2}p) - \delta_z(G^{1/2}G^{13}\bar{p}^{xz}), \tag{3.22}$$

$$\text{PFY} = -\delta_y(G^{1/2}p) - \delta_z(G^{1/2}G^{23}\bar{p}^{yz}), \tag{3.23}$$

and

$$\text{PFZ} + \text{BY} = -\delta_z p + g(\bar{\rho}^z \overline{(\theta'/\Theta)}^z - G^{1/2}\overline{(p/C^2)}^z), \qquad (3.24)$$

where the buoyancy term, BY, was included in (3.24) because of the perturbation pressure term which contributes to ρ'. During actual computations the PFZ + BY term is modified by subtracting off both the horizontally averaged environmental component of θ' as well as the hydrostatic balancing p term. This procedure was found necessary not because of machine precision but because it reduced truncation errors caused by the topographical terms (e.g., [22]). Unrealistic domain-averaged kinetic energy budgets resulted when this procedure was not followed, even though the velocity and potential temperature fields showed no significant change. For the calculations to be presented, this procedure made the difference between counter-gradient heat flux (kinetic energy thermally driven) to gradient heat flux (kinetic energy driven by mesoscale forcing). Thus, for this type of model, it seems imperative to keep the perturbation pressure as small as possible in order to retain the qualitative aspects of the physics.

The Rayleigh friction terms are given as

$$\text{RAYX} = -\bar{\rho}^x(u - (G^{1/2}u)_0/G^{1/2})/\tau_\text{R}, \qquad (3.25)$$

$$\text{RAYY} = -\bar{\rho}^y v/\tau_\text{R}, \qquad (3.26)$$

$$\text{RAYZ} = -\bar{\rho}^z w/\tau_\text{R}, \qquad (3.27)$$

where the mean flow is assumed to be in the x direction with an inflow velocity of $u_0(z)$ at $x = 0$. The main purpose of the Rayleigh friction layer adjacent to the upper lid of the box is to eliminate wave reflection, as stated earlier. To the extent that this numerical devise is efficient the excitation of normal modes of the $\bar{z} = 0$, H domain will also be suppressed.

The diffusion terms are given as

$$\text{KFX} = \delta_x(G^{1/2}\tau_{11}) + \delta_y(\overline{G^{1/2}}^{xy}\tau_{12}) + \delta_z(\tau_{13} + \overline{G^{1/2}G^{13}\tau_{11}}^{xz} + \overline{\overline{G^{1/2}G^{23}}^x\tau_{22}}^z{}^y), \quad (3.28)$$

$$\text{KFY} = \delta_x(\overline{G^{1/2}}^{xy}\tau_{12}) + \delta_y(G^{1/2}\tau_{22}) + \delta_z(\tau_{23} + \overline{\overline{G^{1/2}G^{13}}^y\tau_{12}}^{z}{}^x + G^{1/2}G^{23}\overline{\tau_{22}}^{yz}), \quad (3.29)$$

$$\text{KFZ} = \delta_x(\overline{G^{1/2}}^x\tau_{13}) + \delta_y(\overline{G^{1/2}}^y\tau_{23}) + \delta_z(\tau_{33} + \overline{\overline{G^{1/2}G^{13}}^z\tau_{13}}^z{}^x + \overline{\overline{G^{1/2}G^{23}}^z\tau_{23}}^z{}^y), \quad (3.30)$$

and

$$\text{KFT} = \delta_x(\overline{G^{1/2}}^x H_1) + \delta_y(\overline{G^{1/2}}^y H_2) + \delta_z(H_3 + \overline{G^{1/2}G^{13}\overline{H_1}^z}^x + \overline{G^{1/2}G^{23}\overline{H_2}^z}^y). \quad (3.31)$$

The numerical specifications of D_{ij}, τ_{ij}, H_i, and Def^2 will not be given, as their derivations from the analytical equations in Section 2 are straightforward. The numerical formulations are easily derived, given their respective grid locations from (3.3) to (3.5). The calculation of D_{ij}, K_M, τ_{ij}, and the diffusion terms given in (3.28) to (3.31) represents a significant portion of the computation time during a model run.

Most types of studies will allow a considerable simplication of (3.28) to (3.31) with little loss in accuracy (especially considering the first-order nature of the subgrid scale parameterization). For example when vertical mixing dominates, a common practice is to consider only τ_{13}, τ_{23}, and H_3. The model was coded for the most general case so that sensitivity studies could be performed for the particular physical situation and then the appropriate terms dropped. It is a much simpler procedure to drop terms from a model than to add them, especially when the model is heavily data segmented. The runs presented in this paper considered the full stress tensor, τ_{ij}, as no sensitivity runs have yet been performed.

Before the model equations can be integrated in time we must first specify boundary conditions as well as consider an appropriate scheme for solving the diagnostic pressure equation. The next two sections discuss these points.

3.b. *Boundary Conditions*

The boundary conditons applied at $\bar{z} = 0$, H are taken as

$$\omega = \delta_z(\bar{\rho}^x u) = \delta_z(\bar{\rho}^y v) = 0 \qquad \text{at} \quad \bar{z} = 0, H, \tag{3.32}$$

and in order to allow for the conservation of vertical momentum we also set

$$\overline{\overline{\bar{\rho}^z \omega}^{z} \overline{w}^z}^{z} = 0 \qquad \text{at} \quad \bar{z} = 0, H. \tag{3.33}$$

Equation (3.32) is an approximation to free-slip boundary conditions. A rigorous application of zero tangential vorticity at $\bar{z} = 0$ was avoided because of the complications involved in applying the pressure boundary condition. As will be shown, (3.32) considerably simplifies the pressure boundary condition at $\bar{z} = 0$. Equation (3.33) is a result of the constraint that the vertical integral of ADVZ from $\bar{z} = 0$ to H must vanish.

The boundary conditions for τ_{ij} at $\bar{z} = 0$, H were taken as

$$\overline{\tau_{11}}^z = \overline{\tau_{22}}^z = \overline{\tau_{33}}^z = \overline{\tau_{12}}^z = 0 \qquad \text{at} \quad \bar{z} = 0, \tag{3.34}$$

$$\tau_{13} = \tau_{23} = \delta_z \tau_{22} = \overline{\tau_{33}}^z = \delta_z \tau_{12} = 0 \qquad \text{at} \quad \bar{z} = H, \tag{3.35}$$

and the simple drag law formulations

$$\tau_{13} = \tfrac{1}{2}(\rho/G^{1/2})\, C_d \mid \mathbf{V}_t \mid (u \cos \lambda_x + w \sin \lambda_x)_0 \qquad \text{at} \quad \bar{z} = 0, \tag{3.36}$$

$$\tau_{23} = \tfrac{1}{2}(\rho/G^{1/2})\, C_d \mid \mathbf{V}_t \mid (v \cos \lambda_y + w \sin \lambda_y)_0 \qquad \text{at} \quad \bar{z} = 0 \tag{3.37}$$

were used to model momentum exchange between the air and ground due to frictional drag. On account of the high order of the numerical operators in the stress terms we must also prescribe conditions on τ_{13}, τ_{23} outside the integration domain to ensure that zero stress results at $\bar{z} = H$ and that only (3.36) and (3.37) act to exchange

TERRY L. CLARK

momentum at $\bar{z} = 0$; i.e., we do not want the free convection regime stresses acting at the ground. These conditions are met by

$$\tau_{13}\,(\bar{z} = H + \varDelta z) = \tau_{13}\,(\bar{z} = H - \varDelta z), \tag{3.38}$$

$$\tau_{23}\,(\bar{z} = H + \varDelta z) = \tau_{23}\,(\bar{z} = H - \varDelta z), \tag{3.39}$$

$$\tau_{13}\,(\bar{z} = -\varDelta z) = \left(2\tau_{13}\,(\bar{z} = 0) + \left(\frac{\varDelta z}{2H} - 1\right)\tau_{13}\,(\bar{z} = \varDelta z)\right)\!\Big/\!\left(\frac{\varDelta z}{2H} + 1\right), \tag{3.40}$$

and

$$\tau_{23}\,(\bar{z} = -\varDelta z) = \left(2\tau_{23}\,(\bar{z} = 0) + \left(\frac{\varDelta z}{2H} - 1\right)\tau_{23}\,(\bar{z} = \varDelta z)\right)\!\Big/\!\left(\frac{\varDelta z}{2H} + 1\right). \tag{3.41}$$

In the above equations, λ_x and λ_y are the angles of inclination of the topography in the x and y directions, respectively. $|\,\mathbf{V}_t\,|$ is the magnitude of the tangential velocity at the "zero" level, which is currently taken as one-half the vertical grid point above $\bar{z} = 0$. The above parameterization of momentum exchange at the ground only considers momentum exchange via the τ_{13} and τ_{23} stress tensor components. The contribution due to the other components has been neglected. A more sophisticated formulation for the treatment of boundary layer momentum exchange should be considered in the future.

The turbulent heat flux terms are specified as

$$\overline{H_1^z} = \overline{H_2^z} = 0 \qquad \text{at} \quad \bar{z} = 0, H, \tag{3.42}$$

$$H_3 = 0 \qquad \text{at} \quad \bar{z} = 0, \tag{3.43}$$

and

$$H_3 = \overline{(\rho K_{\mathrm{M}}/G)}^z\,\delta_z\langle\theta'\rangle \qquad \text{at} \quad \bar{z} = H, \tag{3.44}$$

where $\langle\theta'\rangle$ represents the horizontally averaged profile of potential temperature. These conditions are nonconducting at $\bar{z} = 0$. A fixed conduction rate at $\bar{z} = H$ is used to suppress cooling at the very upper regions of the model. The effects of differential heating along sloping surfaces is not considered in the present work although it was the main example treated in [7]. Another boundary condition required is the vertical gradient of K_{M}, which is used to calculate free convective domain mixing. This is given as

$$\delta_z(\rho K_{\mathrm{M}}/G) = 0 \qquad \text{at} \quad \bar{z} = 0, H. \tag{3.45}$$

The only remaining vertical boundary conditions are for the perturbation pressure. These are calculated such that the tendency of ω is zero at both $\bar{z} = 0$ and H. At $\bar{z} = H$ the condition is the usual

$$\delta_z p + gG^{1/2}\overline{(p/C^2)}^z = \mathrm{BP}(x, y, H), \tag{3.46}$$

where $BP(x, y, H)$ represents all of the nonvanishing terms in (3.12) not associated with the pressure. At $\bar{z} = 0$ we must consider all three momentum equations as they apply to the tendency of $\bar{\rho}^z \omega$ through (3.15). We will now see the reason for the simplified form of the free slip boundary condition given by (3.32). This reduces

$$G^{1/2}\delta_t\overline{(\bar{\rho}^z\omega)}^t = OP_{\bar{z}}(\delta_t\overline{(\bar{\rho}^z w)}', \delta_t\overline{(\bar{\rho}^x u)}^t, \delta_t\overline{(\bar{\rho}^y v)}') = 0 \qquad (3.47)$$

to

$$PFZ + gG^{1/2}\overline{(p/C^2)}^z + G^{1/2}\overline{G^{13}PFX}^x + G^{1/2}\overline{G^{23}PFY}^y = BP(x, y, 0) \qquad \text{at} \quad \bar{z} = 0, \qquad (3.48)$$

where PFZ is taken at $\bar{z} = 0$, PFX and PFY are both taken at $\bar{z} = \varDelta z/2$. $BP(x, y, 0)$ is the explicit boundary contritution due to nonpressure terms. Equation (3.48) reduces to an implicit relation between pressures at $\bar{z} = -\varDelta z/2$ and interior fields. For the full three-dimensional calculation (3.48) requires the inversion of a penta-diagonal matrix and the two-dimensional calculation requires the inversion of a tridiagonal matrix. An accurate solution of (3.48) was found necessary in order to prevent mass and energy leakage through the $\bar{z} = 0$ surface. The calculations of two-dimensional flow presented in this paper used a direct method for solving (3.48) which allowed for kinetic energy accountability to round-off error (approximately to the 12th decimal place).

The specification of the lateral boundary conditions is somewhat dependent upon the phenomenon of interest. For simplicity of presentation, only the lateral boundary conditions used in the two-dimensional lee wave calculations will be discussed. (The three-dimensional code still has to be converted from the rather uninteresting x and y cyclic boundary conditions to this case.) A mean flow is considered in the x direction with inflow occurring at $x = 0$ and outflow generally occurring at $x = L$. At the inflow boundary, free slip boundary conditions are used on the various dynamic variables such that

$$\delta_x\theta' = \delta_x w = 0 \qquad \text{at} \quad x = 0, \qquad (3.49)$$

$$u = u_0(z) \qquad \text{at} \quad x = 0, \qquad (3.50)$$

and

$$\overline{[u - u_0(z)]}^x = \overline{u'}^x = 0 \qquad \text{about} \quad x = 0. \qquad (3.51)$$

A Neumann-type boundary condition for the pressure is derived from (3.10) to satisfy the constraint

$$\delta_t\overline{(\bar{\rho}^x u)}^t = 0 \qquad \text{at} \quad x = 0.$$

A zero horizontal gradient is applied to the remaining field variables at $x = 0$. Keeping θ' equal to a fixed upstream profile was found to be numerically unstable when the static stability was large because strong gradients developed which produce unstable $2\,\varDelta x$ vortices. Thus, the potential temperature profile at the inflow boundary column had to allow a certain degree of time variation consistent with the time variation of w at the inflow region. This seems physically reasonable when internal

phase velocities exceed the mean flow speed and consequently influence the temperature profile a finite distance upstream. The ideal result would be an influence at $x = 0$ which is consistent with the larger scale flow far upstream. The present inflow boundary conditions do not rigorously satisfy this condition although their inadequacies are not felt to influence the results presented in this paper significantly. Possibly superior results could be obtained by applying a radiation condition to the perturbation components of the appropriate field variables.

At the outflow lateral boundary extrapolation schemes which approximate a radiation condition are applied to u and θ' for the present calculations. Once an extrapolated future value of $u_{EX}^{\tau+1}$ has been determined at $x = L$, the Neumann condition for pressure is calculated form (3.10) using

$$\delta_t \overline{(\bar{\rho}^x u)}' = \bar{\rho}^\infty (u_{EX}^{\tau+1} - u_L^{\tau-1})/2\Delta t. \tag{3.52}$$

Given extrapolated values of u, θ' and again assuming zero gradients of K_M, τ_{ij} at $x = L$, the solution for p can be obtained which is then used in (3.10) and (3.12) to update u and w. Using an extrapolation scheme consistent with $u_L^{\tau+1}$, $u_{L+\Delta x}^{\tau+1}$ is then determined. The values of $w_{L+\Delta x/2}^{\tau+1}$ are then calculated to satisfy the divergence equation.

The method of extrapolation used at the outflow boundary was, at any height level, to let

$$\phi_L^{\tau+1} = 2\phi_{L-\Delta_1}^{\tau} - \phi_{L-2\Delta_1}^{\tau-1}, \tag{3.53}$$

where Δ_1 is determined as

$$\Delta_1 = \overline{C_{ph}}^\tau \Delta t. \tag{3.54}$$

This method of extrapolation is similar to that used by Orlanski [10]. If $\Delta_1 \neq \Delta x$ then the two variables used in [3.53] are found by linear interpolation in the spatial direction only. The calculation of $\overline{C_{ph}}^\tau (z, t)$ was based on w only, which, as pointed out by Orlanski [10], can lead to some degree of incompatibility between different fields; i.e., the calculation of $\overline{C_{ph}}^\tau$ should really be computed from the field which is being extrapolated. w was chosen because it seemed to give the least amount of incompatibility but still involved the calculation of only one C_{ph} profile. To calculate $\overline{C_{ph}}^\tau$, spatial and time filters were applied near the outflow region as follows. First we calculate C_{ph} by minimizing the functional, ψ,

$$\psi = \sum_{i=NX-3}^{NX-1} \left(\frac{\delta w}{\delta t} + C_{ph} \frac{\delta w}{\delta x} \right)^2, \tag{3.55}$$

with respect to C_{ph}; second we apply the time filter

$$\overline{C_{ph}}^* = \frac{T}{T + \Delta t} \overline{C_{ph}}^{\tau-1} + \frac{\Delta t}{T + \Delta t} C_{ph} \tag{3.56}$$

to obtain the spatial and time-filtered values of $\overline{C_{ph}}^*$. This last $\overline{C_{ph}}^*$ value cannot be used in the extrapolation scheme until some small adjustments are made which allow mass continuity to be retained. Thus, the last step in determining $\overline{C_{ph}}^\tau$ was to let

$$\overline{C_{ph}}^\tau = \overline{C_{ph}}^* + C_{ph}', \tag{3.57}$$

where C_{ph} is calculated in the least-squares sense to ensure that extrapolated values of horizontal velocity have the correct column mass flux. If this last procedure is not followed, the pressure equation becomes ill-posed and the model will eventually become numerically unstable.

This completes the description of the basic equations and boundary conditions required to obtain a solution of the governing equations. The method of solving for the pressure will now be discussed. In order to be general, the pressure solution technique used for the full three-dimensional code of the model will be described.

4. Diagnostic Pressure Equation

A divergence equation derived from (3.10) to (3.13) using the definition of ω as defined in (3.15) results in a diagnostic pressure equation which can be solved using the appropriate boundary conditions. Using the operator defined in (3.16), this divergence equation has the general form

$$\delta_x[\delta_t(\overline{\rho^x u})'] + \delta_y[\delta_t(\overline{\rho^y v})'] + (1/G^{1/2})\,\delta_z[OP_{\tilde{z}}(\delta_t\overline{\rho^z w}', \delta_t\overline{\rho^x u}', \delta_t\overline{\rho^y v}')]$$

$$= \delta_t\overline{DV}^t = -DV^{\tau-1}/2\Delta t, \tag{4.1}$$

where the desired result of $DV^{\tau+1} = 0$ has been employed. The $DV^{\tau-1}$ term is retained in order to provide a negative feedback on momentum divergence error growth as suggested by Harlow and Welch [14]. Separating pressure terms from the remaining terms, (4.1) can be written as the diagnostic pressure equation

$$\delta_x(PFX) + \delta_y(PFY) + (1/G^{1/2})\,\delta_z[OP_{\tilde{z}}(PFZ, PFX, PFY)] - g\delta_z\overline{(p/C^2)}^z = F(x), \tag{4.2}$$

where F contains the divergence of advective, diffusive, buoyancy, Coriolis, and Rayleigh friction terms. In the actual model F is calculated by applying the operator, $OP_{\tilde{z}}$, and applying horizontal divergence to the appropriate terms in (3.10) and (3.11). For the three-dimensional model (4.2) represents a 25-point operator on pressure, whereas for the two-dimensional model it represents a 15-point operator. Inspection of (4.2) together with the vertical boundary conditions (3.46) and (3.48) reveals that the solution of p requires the solution of a rather complicated equation. A double-iteration scheme, where the outer interation involves breaking the interior pressure operator up into an implicit and an explicit component with the explicit component of higher order, was found to be reasonably efficient. The same procedure is applied

to the specification of the vertical pressure boundary conditions. More specifically the outer interation calculates (4.2), (3.46), and (3.48) as

$$G\nabla_{H}^{2}\phi + \delta_{zz}\phi = G \cdot F + Lp^{*} = Q, \qquad (4.3)$$

$$\phi_{ij1} = \phi_{ij2} + \beta_{0}(p^{*}), \qquad (4.4)$$

$$\phi_{ijNZ} = \phi_{ijNZ-1} + \beta_{H}. \qquad (4.5)$$

where $\phi = G^{1/2}P$, p^{*} is the most current value of p; L is the explicit portion of the total pressure operator; β_{0} is the explicit lower boundary condition at $\bar{z} = 0$, which is a weak function of p^{*}; and β_{H} is the explicit upper boundary condition at $\bar{z} = H$, which is independent of p^{*}.

The inner iteration consists of using the dimension reduction method of Ogura [17] to transform (4.3) through (4.5) to a set of decoupled horizontal Helmholtz equations which can be solved by either direct or efficient iterative schemes. Letting $\mathscr{S}$ be the column matrix of ϕ, the equations become

$$\Delta z^{2} G\nabla_{H}^{2}\mathscr{S} + \mathscr{A}\mathscr{S} = \mathscr{H}, \qquad (4.6)$$

where the transpose of $\mathscr{S}$ is given as

$$\mathscr{S}^{\mathrm{T}} = [\phi_{ij2}, \phi_{ij3}, ..., \phi_{ijNZ-1}] \qquad (4.7)$$

and

$$\mathscr{H}^{\mathrm{T}} = [\Delta z^{2} q_{ij2} - \beta_{0ij}, \Delta z^{2} q_{ij3}, ..., \Delta z^{2} q_{ijNZ-2}, \Delta z^{2} q_{ijNZ-1} - \beta_{Hij}] \qquad (4.8)$$

and the matrix $\mathscr{A}$ is defined as

$$\mathscr{A} = \begin{pmatrix} -1 & 1 & 0 & & & & & 0 \\ 1 & -2 & 1 & 0 & & & & \\ 0 & 1 & -2 & 1 & & & & \\ & & & & 1 & -2 & 1 & 0 \\ & & & & & 1 & -2 & 1 \\ 0 & & & & & & 1 & -1 \end{pmatrix}. \qquad (4.9)$$

Letting $\mathscr{T}$ and $\mathscr{T}^{\mathrm{T}}$ represent the eigenvector and inverse eigenvector matrices of $\mathscr{A}$, (4.6) is then transformed to

$$\Delta z^{2} G\nabla_{H}^{2}\mathscr{P} + \mathscr{D}\mathscr{P} = \mathscr{R}, \qquad (4.10)$$

where

$$\mathscr{P} = \mathscr{T}\mathscr{S} \qquad (4.11)$$

and

$$\mathscr{D} = \mathscr{T}\mathscr{A}\mathscr{T}^{\mathrm{T}} \qquad (4.12)$$

is the diagonal eigenvalue matrix. Converting the lateral pressure boundary conditons to a form consistent with $\mathscr{P}$ we can then solve the complete set of Helmholtz equations given by (4.10). There is one zero eigenvalue in (4.12) corresponding to the fact that

the Neumann boundary conditions do not allow a unique solution to (4.3). The procedure used to force uniqueness was to set the value of $\mathscr{P}$ corresponding to the zero eigenvalue equal to zero at $x = -\varDelta x/2$. The method used to force uniqueness is not important since this part of the solution corresponds to the homogeneous pressure solution, which by definition has no dynamic significance. Should the solution for p obtained to this point not be accurate enough then we go back to Eq. (4.3), replace p^* by the newly calculated values, and go through the entire procedure again. After the last complete iteration (3.48) is explicity solved for pressures at $\bar{z} = -\varDelta z/2$ in order to ensure that $\omega = 0$ is accurately satisfied at $\bar{z} = 0$.

The number of outer iterations required is a function of the time resolution as well as the number of vertical grid levels. For $NZ = 42$ the two-dimensional model required only two outer iterations whereas when NZ was increased to 82, three outer iterations were required for the 1-km mountain case.

5. Momentum Budget of Model

A spatial integration over the model domain for the x-direction momentum equation results in

$$\frac{\partial}{\partial t} \oint \rho u \, dx \, dy \, d\bar{z} = - \oint (\rho u^2 + G^{1/2}p - G^{1/2}\tau_{11})|_{x=0}^{L_x} \, dy \, d\bar{z}$$

$$- \oint \left(p \frac{\partial z_s}{\partial x} + \tau_{13} \right) dx \, dy - \oint \rho u'/\tau_R \, dx \, dy \, d\bar{z}, \qquad (5.1)$$

where the first integral on the right-hand side of (5.1) represents all the terms acting at the lateral x-direction boundary. The y-direction has been taken as cyclic in this section for simplicity of presentation. The second integral on the right-hand side of (5.1) represents the combined effects of wave and surface frictional drag. The third integral represents the loss of momentum due to the Rayleigh friction terms. A similar equation results for the y-direction momentum. The volume integral of ρu for the model is approximated using a linear quadrature such that the integration domain is identical to that used in (5.1). The numerical equations of the model which approximate (5.1) are then

$$\sum_{k=2}^{NZ-1} \sum_{j=2}^{NY-1} \sum_{i=1}^{NX-1} \gamma_i \delta_t \overline{(\bar{\rho}^x u)}^t \, \varDelta x \, \varDelta y \, \varDelta \bar{z}$$

$$= -\text{UFYZ} - \text{UPYZ} + \text{USTYZ} - \text{UPXY} - \text{USTXY} - \text{URAY}, \qquad (5.2)$$

where UFYZ, UPYZ, and USTYZ represent the differential domain momentum flux, pressure gradient force (mesoscale pressure force), and normal stress occurring at the YZ planes of the model domain, respectively. UPXY and USTXY represent the wave drag and surface frictional stress, respectively, and URAY represents the momentum loss due to the Rayleigh friction terms. The γ_i term in (5.2) is equal to unity for $i = 2, 3,..., NX - 2$ and is equal to 0.5 when $i = 1$ or $NX - 1$. This

simply defines the integration quadrature. The numerical forms of the respective terms in (5.2) are found to be

$$\text{UFYZ} = \sum_k \sum_j \left[\overline{(\overline{\bar{\rho}^x u}^x \bar{u}^x)}^x \big|_{i=1}^{NX-1} \right] \Delta y\, \Delta \bar{z}, \tag{5.3}$$

$$\text{UPYZ} = \sum_k \sum_j \left[\overline{(G^{1/2} p)}^x \big|_{i=1}^{NX-1} \right] \Delta y\, \Delta \bar{z}, \tag{5.4}$$

$$\text{USTYZ} = \sum_k \sum_j \left[\overline{(G^{1/2} \tau_{11})}^x \big|_{i=1}^{NX-1} \right] \Delta y\, \Delta \bar{z}, \tag{5.5}$$

$$\text{UPXY} = \sum_i \sum_j \gamma_i (\bar{p}^{xz} \delta_x z_s)\, \Delta x\, \Delta y \qquad \text{for} \quad \bar{z} = 0, \tag{5.6}$$

$$\text{USTXY} = \sum_i \sum_j \gamma_i \tau_{13}\, \Delta x\, \Delta y \qquad \text{for} \quad \bar{z} = 0, \tag{5.7}$$

and

$$\text{URAY} = -\sum_i \sum_j \sum_k \gamma_i (\bar{\rho}^x u' / \tau_{\mathbf{R}})\, \Delta x\, \Delta y\, \Delta \bar{z}. \tag{5.8}$$

The terms given by (5.3) to (5.8) will be displayed in a time-integrated sense, which is denoted by a "T" preceding each term.

A spatial integration over the model domain for the vertical momentum results in the six source/sink terms

$$\frac{\partial}{\partial t} \oint \rho w\, dx\, dy\, d\bar{z} = - \oint (\rho u w - G^{1/2} \tau_{13}) \big|_{x=0}^{L_x} dy\, d\bar{z}$$

$$- \oint p \big|_{\bar{z}=0}^{H} dx\, dy + \oint \left(\tau_{13} \frac{\partial z_s}{\partial x} + \tau_{23} \frac{\partial z_s}{\partial y} \right) \Big|_{z=0} dx\, dy$$

$$+ \oint \left[g\left(\rho \frac{\theta'}{\Theta} - G^{1/2} \frac{p}{C^2} \right) - \rho w / \tau_{\mathbf{R}} \right] dx\, dy\, d\bar{z}. \tag{5.9}$$

These six source/sink terms are found from the model equations to be

$$\sum_i \sum_j \sum_k \gamma_k (\delta_t \overline{\bar{\rho}^z w}')$$

$$= -\text{WFYZ} + \text{WSTYZ} - \text{WPXY} + \text{WSTXY} + \text{WBY} - \text{WRAY}, \tag{5.10}$$

where

$$\text{WFYZ} = +\sum_j \sum_k \gamma_k \left[\overline{(\overline{\bar{\rho}^x u}^z \overline{w}^x)} \big|_{i=1}^{NX-1} \right] \Delta y\, \Delta \bar{z}, \tag{5.11}$$

$$\text{WSTYZ} = \sum_j \sum_k \gamma_k \left[\overline{(G^{1/2}}^x \tau_{13}) \big|_{i=1}^{NX-1} \right] \Delta y\, \Delta \bar{z}, \tag{5.12}$$

$$\text{WPXP} = +\sum_i \sum_j \bar{p}^z \big|_{\bar{z}=0}^{H} \Delta x\, \Delta y, \tag{5.13}$$

$$\text{WSTZY} = +\sum_i \sum_j \left[\overline{(\tau_{13} \delta_x z_s)}^x + \overline{(\tau_{23} \delta_y z_s)}^y \right] \big|_{\bar{z}=0} \Delta x\, \Delta y, \tag{5.14}$$

$$\text{WBY} = +\sum_i \sum_j \sum_k \gamma_k \left[g(\bar{\rho}^z \overline{(\theta'/\Theta)}^z - G^{1/2} \overline{(p/C^2)}^z \right] \Delta x\, \Delta y\, \Delta \bar{z}, \tag{5.15}$$

and

$$\text{WRAY} = \sum_i \sum_j \sum_k \gamma_k \bar{\rho}^z w / \tau_R \, \Delta x \, \Delta y \, \Delta \bar{z}, \tag{5.16}$$

with $\gamma_k = 1$ for $k = 2, 3,..., NZ - 2$ and $\gamma_k = 0.5$ for $k = 1$ or $NZ - 1$. All of the source/sink terms of the model have equivalent physical terms in the analytical equations for both the horizontal and the vertical momentum. It is common knowledge that this is not the case for the kinetic energy source/sink terms, which will be described for the model in the next section.

6. KINETIC ENERGY OF THE MODEL

The grid value kinetic energy, ke_{ijk}, is defined as

$$ke_{ijk} = (\overline{\bar{\rho}^x u^2}^x + \overline{\bar{\rho}^y v^2}^y + \overline{\bar{\rho}^z w^2}^z)/2, \tag{6.1}$$

which defines the kinetic energy at the grid center. The tendency equation for ke is found by multiplying (3.10) to (3.12) by $\tilde{u}$, $\tilde{v}$, and $\tilde{w}$ and taking grid averages in the x, y, and $\bar{z}$ directions, respectively. The "$\sim$" represents a time average where, for example, $\tilde{u} = (u^{\tau+1} + u^{\tau-1})/2$. The resulting tendency equation for ke is found as

$$\delta_t \overline{ke}^t = - \text{ADVKE} - \text{DIVPV} + \text{CPK} + \text{DIFTRNS} + \text{DISS} + \text{RKE}$$
$$+ \{\text{CKI} + \text{NLADV} + \text{PTR}\}, \tag{6.2}$$

where the terms on the right-hand side represent advection of ke, the pressure work term, conversion from potential to kinetic, diffusional transfer, dissipation, Rayleigh friction, conversion from kinetic to internal, nonlinear advective generation, and a pressure truncation error term, respectively. The terms in brackets are those terms which have no physical equivalent terms in the analytical equations. The Ogura and Phillips [3] deep equations do not have any conversion from kinetic to internal by virtue of the fact that the base state is taken as a dry isentropic atmosphere. NLADV terms are due to the nonconservative nature of the centered time-differencing scheme for the nonlinear advection terms. The last nonphysical term arises through a slight imbalance (in the model) between pressure terms which transfers kinetic energy from that associated with motion in the x direction (say) to that associated with motion in an orthogonal direction. To clarify this point consider the kinetic energy equations for u^2 and w^2 where we find

$$\frac{\partial}{\partial t}(\rho u^2/2) = -\frac{\partial}{\partial x}(G^{1/2} pu) + p\frac{\partial}{\partial x}(G^{1/2} u) - uG^{1/2}G^{13}\frac{\partial p}{\partial \bar{z}} + \cdots \tag{6.3}$$

and

$$\frac{\partial}{\partial t}(\rho w^2/2) = -\frac{\partial}{\partial \bar{z}}(G^{1/2} p\omega) + p\frac{\partial}{\partial \bar{z}}(G^{1/2}\omega) + uG^{1/2}G^{13}\frac{\partial p}{\partial \bar{z}} + \cdots. \tag{6.4}$$

The last terms of (6.3) and (6.4) convert kinetic energy between $\rho u^2/2$ and $\rho w^2/2$. The difference between the numerical formulation of these terms in the horizontal and vertical kinetic energy equations gives rise to the pressure truncation error, PTR.

The numerical equations for the various terms are

$$\text{ADVKE} = \delta_x[\overline{\bar{\rho}^x u}^x(\overline{\tilde{u}\,u}^{x-x} - \overline{u^2}^x/2)^x + \overline{\bar{\rho}^x u}^y(\overline{\tilde{v}\,v}^{x-x} - \overline{v^2}^x/2)^y$$

$$+ \overline{\bar{\rho}^x u}^z(\overline{\tilde{w}\,w}^{x-x} - \overline{w^2}^x/2)^z\,] + \cdots, \tag{6.5}$$

$$\text{DIVPV} = \delta_x(\overline{G^{1/2}\tilde{u}\bar{p}^x}^x) + \delta_y(\overline{G^{1/2}\tilde{v}\bar{p}^y}^y) + \delta_z(G^{1/2}\tilde{\omega}\bar{p}^z), \tag{6.6}$$

$$\text{CPK} = g\bar{\rho}^z\overline{(\theta'/\Theta)}^z\tilde{w} \tag{6.7}$$

$$\text{DIFTRNS} = \delta_x(\overline{G^{1/2}\tau_{11}}^x\tilde{u}) + \delta_y(\overline{G^{1/2}}^{xy}\tau_{12}\bar{u}^y)$$

$$+ \delta_z\bar{u}^z(\tau_{13} + G^{1/2}G^{13}\overline{\tau_{13}}^x + \overline{G^{1/2}G^{23}}^x\overline{\tau_{12}}^{y}{}^z)$$

$$+ \cdots, \tag{6.8}$$

$$\text{DISS} = - G^{1/2}\tau_{11}\delta_x\tilde{u} - \overline{G^{1/2}}^{xy}\tau_{12}\delta_y\tilde{u}^{xy} - \tau_{13}\delta_z\tilde{u}$$

$$- \overline{G^{1/2}G^{13}\tau_{11}}^{xz}\delta_z\tilde{u} - \overline{G^{1/2}G^{23}}^x\overline{\tau_{12}}^{y}{}^{xz}\delta_z\tilde{u}$$

$$- \cdots, \tag{6.9}$$

$$\text{RKE} = - \overline{\bar{\rho}^x\tilde{u}u'/\tau_R}^x - \overline{\bar{\rho}^v\tilde{v}v'/\tau_R}^y - \overline{\bar{\rho}^z\tilde{w}w/\tau_R}^z, \tag{6.10}$$

$$\text{CKI} = p[\delta_x(\overline{G^{1/2}}^x\tilde{u}) + \delta_y(\overline{G^{1/2}}^y\tilde{v}) + \delta_z(G^{1/2}\omega)] - g\tilde{w}\overline{(p/C^2)}^z, \tag{6.11}$$

$$\text{NLADV} = - \overline{(u^2/2)\,\overline{DV}^x}^x - \overline{(v^2/2)\,\overline{DV}^y}^y - \overline{(w^2/2)\,\overline{DV}^z}^z$$

$$+ [\overline{\bar{\rho}^x u}^x\bar{u}^x\delta_{xtt}u^{xx} + \overline{\bar{\rho}^x\omega}^x\bar{u}^z\delta_{ztt}u^{xz} + \cdots]\,\Delta t^2/2, \tag{6.12}$$

and finally the pressure truncation error term is

$$\text{PTR} = - \overline{\tilde{u}G^{1/2}G^{13}\delta_z\bar{p}^{x}}^{z}{}^x + [(\overline{G^{1/2}G^{13}\bar{\rho}^x\tilde{u}}^x\,\delta_zp)\cdot(\bar{\rho}^2)^{-1}]^z$$

$$- \overline{\tilde{v}G^{1/2}G^{23}\delta_z\bar{p}^{y}}^{z}{}^y + [(\overline{G^{1/2}G^{23}\bar{\rho}^v\tilde{v}}^y\,\delta_zp)\cdot(\bar{\rho}^2)^{-1}]^z. \tag{6.13}$$

Strictly speaking (6.11) is not purely a conversion from kinetic to internal energy because of the addition of the pressure perturbation component of the CPK term. In the form presented in (6.10), CKI should be zero to within truncation error.

A time and spatial integral of (6.2) leads to

$$\Delta \text{ KE} = \text{TFLUX} + \text{TPWRK} + \text{TCPK} + \text{TDISS} + \text{TRKE} + \text{TTPR}$$

$$+ \text{ lower-order terms,} \tag{6.14}$$

where for the calculations to be presented the lower-order terms are at least an order of magnitude smaller than the smallest of the other seven terms. The accountability of the total change of Δ KE was found to exist to the 10th to 12th decimal place after as many as 800 time steps. This level of accountability was used to trace coding errors in the model. By explicitly calculating *all* of the terms in (6.2) using a code which was independent of the "data generator" code, the coding errors of the model were eliminated by demanding a round-off balance at each grid point of the model. This balance was achieved for the most general case of $NX \neq NY \neq NZ$ and $\Delta x \neq \Delta y \neq \Delta z$. The terms on the right hand side of (6.14) represent the time-integrated flux of kinetic energy through the domain, the work performed by the pressure field at the domain boundaries, the total conversion from potential to kinetic energy, the total dissipation (ρu^2 disspation will be denoted separately as TDISSX), total loss due to Rayleigh friction (again the ρu^2 component will be denoted as RKEX), and the nonphysical pressure truncation error loss (this term usually acts as a sink).

This completes the description of the model equations. The subsequent section will discuss the physical phenomenon of airflow over a ridge, studied using this model

7. Results

Two cases of topography are considered using the "Witch of Agnesi" (see [19, p. 518]),

$$z_s = a^2 h/(a^2 + x^2), \tag{7.1}$$

with the mountain half-width, a, equal to 3 km and $h = 100$ m and 1 km. The atmospheric stability and mean flow are taken as

$$d\bar\theta/dz = 3K/\text{km}, \tag{7.2}$$

$$U_0 = 4 \text{ m/sec}, \tag{7.3}$$

$$\omega = DV = 0, \tag{7.4}$$

where U_0 is the domain inflow velocity. A nondimensional number which is important to this problem is the inverse Froude number, F, based on the ratio of the wave-launching period to the Brunt Vaisala period, where

$$F = T_f/T_n = (a/U)/(2\pi/(gS)^{1/2}) = 1.18. \tag{7.5}$$

TERRY L. CLARK

S is the static stability parameter, which is equal to the logarithmic derivative with height of the environmental potential temperature. Linear theory predicts freely propagating waves when when $F > 1$, provided there is a radiation condition allowing wave energy to propagate to infinity. The numerical model uses Rayleigh friction in the top five levels of the model with $\tau_R = (800, 400, 200, 100, 100)$ sec and decreasing τ_R with increasing height in order to simulate a radiation condition at the model's lid, $\bar{z} = H$.

The grid resolutions used were $\Delta x = 600$ m for all cases, and $\Delta z = 100$ m or 200 m depending on the particular run. Table I lists the various runs performed with the numerical model. NZ, NX are the number of vertical and horizontal grid points, respectively. I_0 is the position in x about which the topography is centered. Run 18 is the only case where no surface frictional drag was considered. All other cases used $C_d = 0.001$ in (3.36). Runs 14 and 18 have the small mountain height of 100 m, whereas all other runs have a mountain height of 1 km.

TABLE I

Description of Runs

Run	h	Δz	(NZ, NX)	I_0	Comments
14	100 m	100 m	(82, 62)	31.5	
18	100 m	100 m	(82, 62)	31.5	$\tau_{13} = 0$
15	1 km	100 m	(82, 62)	31.5	
16	1 km	200 m	(82, 62)	31.5	
19	1 km	200 m	(42, 62)	31.5	
21	1 km	200 m	(42, 92)	46.5	
17	1 km	200 m	(42, 122)	61.5	
22	1 km	200 m	(42, 122)	91.5	

The 100 m mountain calculations are compared with linear theory in order to assess the performance of the numerical model. To do this, linear theory calculations were supplied by Peltier [18]. These calculations were based on a full linearization of the fluid flow as well as on the treatment of the lower boundary conditions, i.e.,

$$w(x, 0) = U(0)(\partial h/\partial x).$$

A description of this linear theory can be found in [20] for the constant stability case. Figure 1A shows the near-steady-state field plot of w for run 18. The time level shown is $t = 4000$ sec. Many of the field characteristics of Fig. 1A are in good agreement with linear theory, as shown in Fig. 1b. The vertical wavelength of the w modes is approximately 7 % larger for the nonlinear model than predicted by linear theory. This slight difference could be due to vertical resoltuion, nonlinearities, or some slight differences in the internal physics between the nonlinear model and linear theory. It is encouraging to see the numerical model reproducing the detail of the w modes in the upper levels of the domain. We see the development of secondary maxima of w,

which is in agreement with linear theory. Two strong differences between this nonlinear calculation and linear theory, however, are quite apparent. The first is the considerably reduced intensity of the w modes for Run 18 below that predicted by linear theory and the second is the marked asymmetry of $|w|$ about the mountain at $\bar{z} = 0$. These two differences are attributed to the combined effects of the nonlinear lower boundary condition and the eddy mixing.
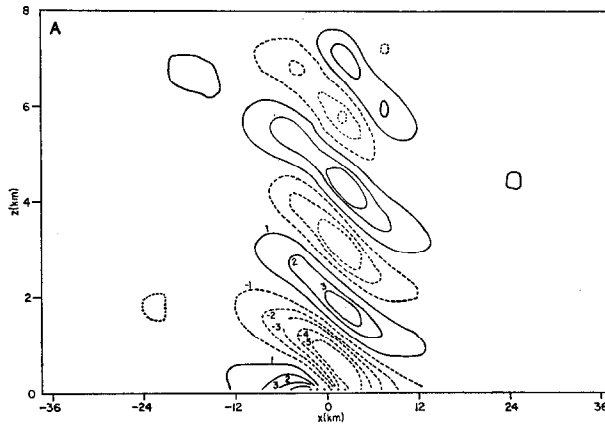

FIG. 1A. Vertical velocity field, w. for run 18 at $t = 4000$ sec. Contour interval is 0.02 msec^{-1}. The stippled area represents the ground.
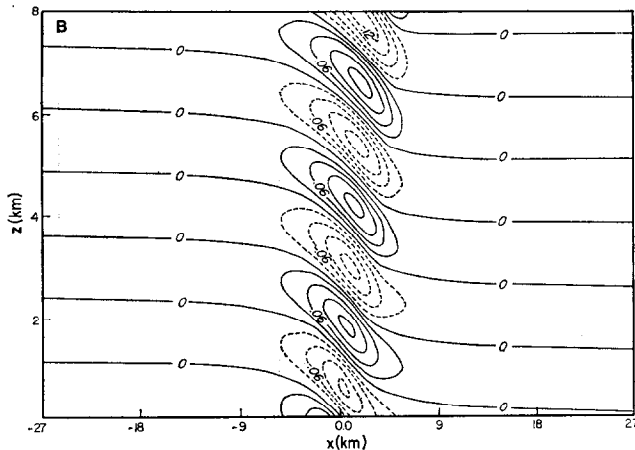
FIG. 1B. Same as Fig. 1A except for the steady-state linear solution. The contour interval is 0.03 msec^{-1}.

The marked decrease in the intensity of w with height which is evident in Fig. 1A is due to the strong eddy mixing to which the flow has been subjected. Subsequent to the initial calculations described here, the model has been run for the case $h = 100$ m

with $K_M = 0$. In this case the asymmetry of $|w|$ at $\bar{z} = 0$ about the mountain remains. However, beyond a critical height above the crest of the topography the maximum amplitude of successive phases of w becomes constant and the comparison with linear theory in this region significantly improves in consequence. The effects of K_M and of its parameterization are a subject of current study. The results of this study will be discussed elsewhere.

Runs 14 and 18 showed only slight differences, which are attributed to the effects of including a surface frictional drag. Run 14 had lower tangential winds at $\bar{z} = 0$ and a lower wave drag value. These differences were only slight and all qualitative aspects of the calculations remained unchanged. The comparison of these two experiments clearly indicates that the surface frictional drag had no significant influence on the overall results.

Figure 2 displays w for run 15 at $t = 4000$ sec. The effect of the nonlinear lower boundary condition is now quite pronounced. There is a rather strong downslope wind component in the lee of the mountain. The asymmetry of $|w|$ is still apparent for this case. A detailed comparison shows that the degree of asymmetry has slightly increased from runs 14 and 18. In Fig. 2 we still see the upper-level modes of w indicating the vertical propogation of momentum. The intensity of w in these upper levels has increased by a factor of 16 over run 18 even though h has been increased by a factor of 10. (The linear theory predicts the field variables as being proportional to h.) Figure 2 is the first indication that the effects of the nonlinear lower boundary condition may play a significant role in the downslope wind problem. The calculations and analysis presented in this paper are not extensive enough to warrant any final conclusions in this respect.
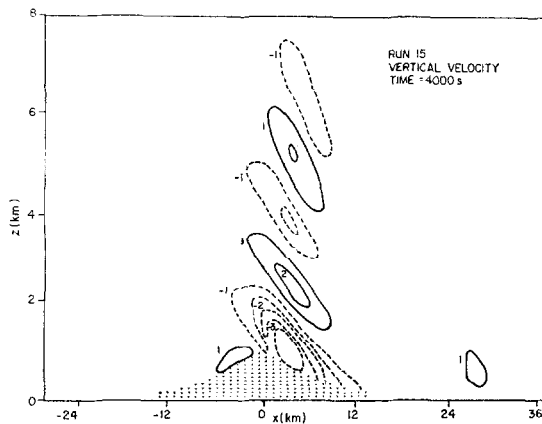

FIG. 2.   Same as Fig. 1 except for run 15. The contour interval is 0.5 msec^{-1}.

The wave drag values, $D_{\overline{w}}$ ($= -$UPXY), from the nonlinear model were calculated for all runs. The 100 m mountain case resulted in $D_{\overline{w}} = -294.4$ and -316.5 kg sec^{-2} for runs 14 and 18, respectively. The linear theory (which has a closer physical corre-

spondence with run 18) resulted in $D_w = -305.0$ kg sec^{-2}. Thus, the numerical model is able to reproduce wave drag values accurately which closely correspond to analytical values when h is small. The effect of the nonlinear treatment of the lower boundary condition did not affect the magnitude of the total wave drag for this particular case of a 3 km half-width and an aspect ratio of 1/30.

The wave drag values for runs 19, 21, 17, and 22 were found to be about three times larger than predicted from analytic linear theory. Before discussing the actual values of D_w from these runs I think it is worth discussing the purpose of these four runs. From Table I we see that the main difference among these runs is the lateral extent. If the inflow and outflow lateral boundaries are not significantly affecting the results, then an asymptotic approach to a converged solution should be expected. The initial conditions described as "shock" start-up did not result in any detectable degree of convergence for $| D_w |$ for these runs. The effect of the excited transients was to cause a gradual (although still at the 20 % level of total change between runs 19 and 22) reduction with increasing L. This reduction of $|D_w|$ was found to vary linearly with the upstream distance to the inflow boundary. A recalculation of the first three runs with a 100 Δt gradual start-up of the mean flow eliminated both the transients as well as the convergence problem. Over the first 100 Δt the mean flow was increased by 1 % of its final value at each time step. The D_w values obtained from this smooth start-up procedure were $D_w = -1.00$, -0.910, and -0.900×10^5 kg sec^{-2} for runs 19, 21, and 17, respectively. These numbers correspond to an asymptotic value of $D_w = 0.899 \times 10^5$ kg sec^{-2} with an "e" folding upstream distance of approximately 4 km. Since linear theory calculates $D_w \sim h^2$, the combined effects of the nonlinear treatment of the lower boundary condition as well as the nonlinear treatment of the fluid flow result in an increase of $| D_w |$ by a factor of about 3 over linear theory. This increase can be further supported as being physical because the effect of increasing the vertical resolution was to cause a further increase in $| D_w |$; i.e., Run 15 gave larger $| D_w |$ values than were obtained in run 19. Unfortunetaly, the sensitivity of the D_w values to the start-up procedure was not recognized until the very late stages of this project so that run 15 was only calculated for a shock start-up case. Even so, a comparison of runs 15 and 19 for the same start-up procedure seems justified for isolating the qualitative effects of vertical resolution.

Figures 3A and 3B show an early time sequence of θ' field plots for run 17 with a shock start-up procedure. The shock start-up produces transients which propagate downstream and, to a lesser extent, upstream. A good test of the radiation outflow condition is that these transients can easily pass through the outflow boundary with no significant reflections. In these two figures we see a very weak warm front propagating downstream at approximately 9.3 m sec^{-1}. The last time sequence in Fig. 3B shows a leveling-off of the θ' contours, which do not show any reflections in the later stages of the calculations. (The calculations were carried to 200 min.) We can also see the low-level warming in the lee of the mountain caused by adiabatic warming associated with the downslope winds.

Figure 4 shows the vertically averaged phase velocities versus t for the shock start-up runs. A peak value of $\bar{C}^z_{\text{phs}}$ is reached as the transients reach the outflow
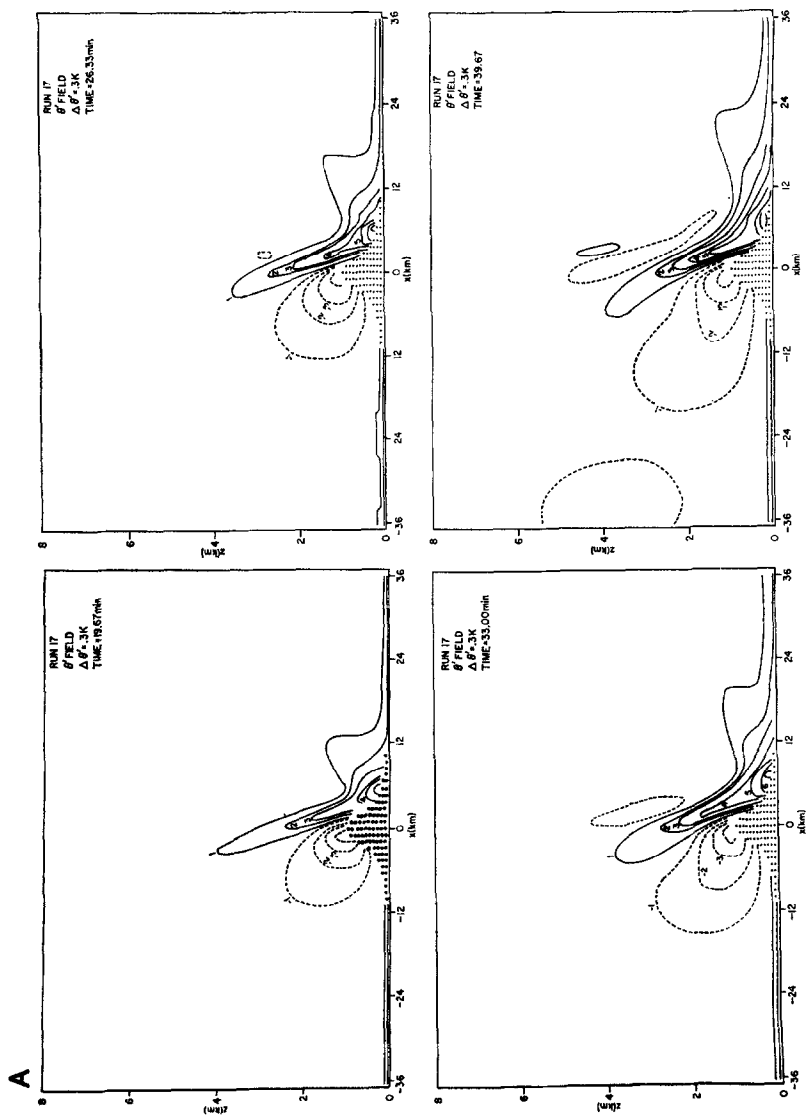
Fig. 3A. Field plot of θ' for run 17 at four consecutive times. The contour interval is 0.3K.
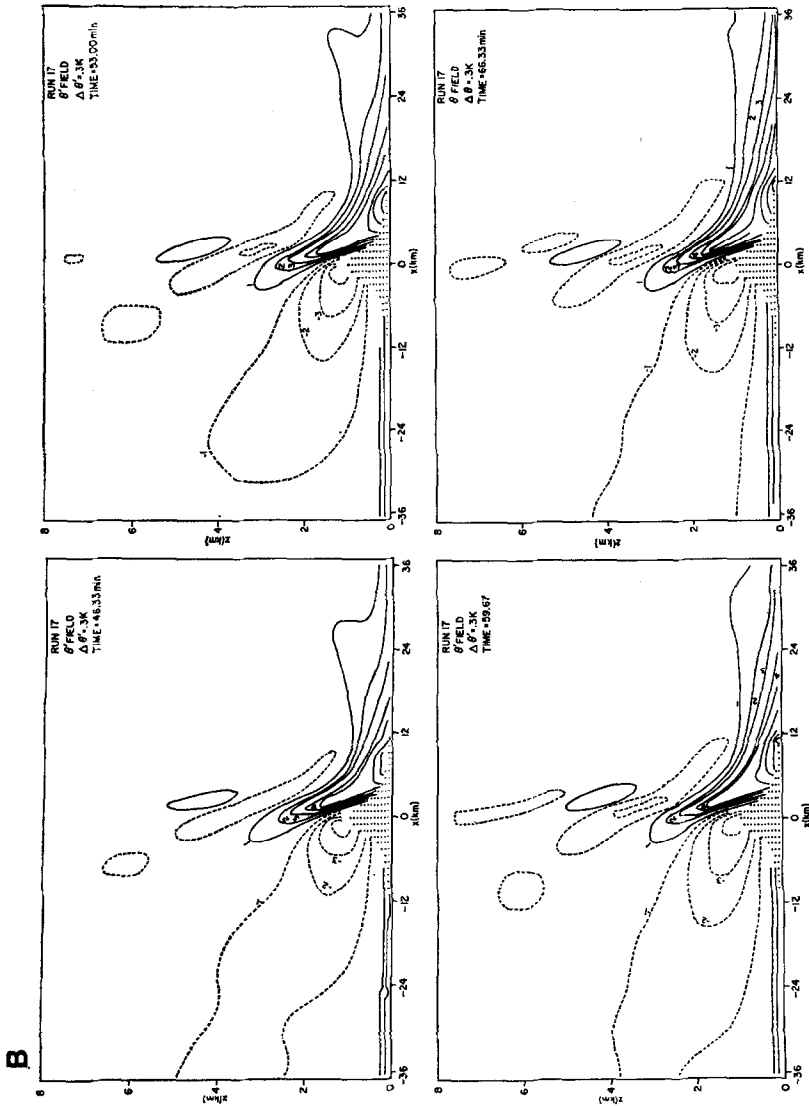
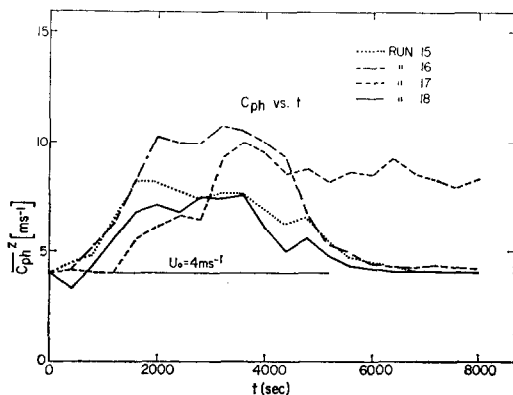FIG. 3B. Same as Fig. 3A except for four later times.

FIG. 4. Vertically averaged "phase" velocities versus t used in extrapolation scheme at the outflow boundary. Shock start-up cases.

boundary and die off with their passing. Run 17 values have not decayed back to 4 m sec^{-1} because of the increased lateral extent. In Fig. 5 a clear indication of the reduced transients in the 100 Δt smooth start-up calculations can be seen in the $\bar{C}^z_{phs}$ versus t plots for runs 19, 21, and 17. For run 19 there appears to be no indication of downstream transients, whereas with increasing downstream extent there is a tendecy toward an increased level of transients.
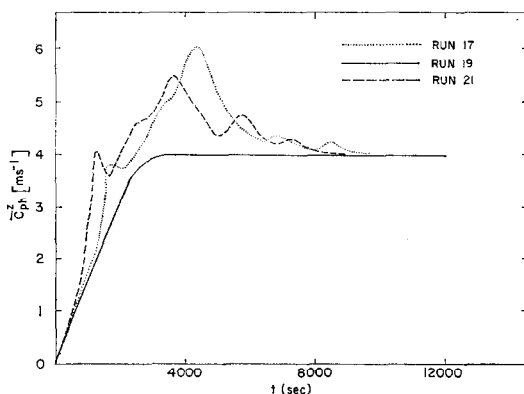
FIG. 5. Same as Fig. 4 except for smooth start-up cases.

Figure 6 shows the energy budget for run 16 with shock start-up. This plot is representative of all the cases treated. We can see that the total change in kinetic energy has balanced off to a steady-state. The only source term in this time and spatial domain-integrated source/sink terms is the mesoscale pressure work. All other physical terms act as sinks to ΔKE. The Rayleigh friction in the x direction is at the 10 % level, whereas the pressure truncation error term does not appear in the figure because it is about 3 octals below ΔKE. The nonlinear instability terms arising through the
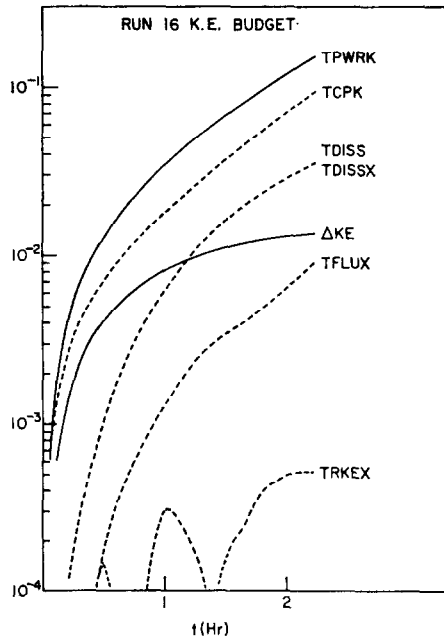
FIG. 6.   Kinetic energy budget for run 16.

numerical treatment of advection are another octave below the pressure truncation error term. The model's budget is clearly dominated by the physical terms with the truncation error terms remaining at a very low and acceptable level. As was already stated, the total ΔKE is accounted for the 11th decimal.

8. CONCLUSIONS

A three-dimensional numerical model with a coordinate transformation allowing an exact treatment of the surface boundary condition of zero normal mass flux has been described. The second-order finite-difference approximations of the equations allowed for good momentum and kinetic energy budgets. The nonphysical source/sink terms for kinetic energy were found for the examples treated to be at least three orders of magnitude smaller than the physical terms.

The generalized Kreiss radiation boundary condition at the lateral outflow boundary performed well for the two-dimensional mountain wave calculations. This boundary condition worked well even when significant transient waves were excited by a shock start-up procedure.

The application of the model to wave drag studies indicated the importance of a proper treatment of the surface boundary condition. Some important aspects of linear theory were simulated by the nonlinear model, such as total wave drag for the 100 -m

mountain case, the vertical wavenumber of the propagating modes, and the detailed structure of the "w" field in the upper levels of the domain. These similarities give a certain degree of credibility to the model and suggest an added importance of the differences between linear theory which were found for the particular geometry and mean flow conditions considered. For the case of constant stability and no shear mean flow, where the launching period of the waves (mountain half-width/mean flow speed) is only slightly larger than that of the Brunt Väisälä period and where a small half-width scale of 3 km is assumed, it was found that a nonlinear treatment of the lower boundary conditions results in a high degree of assymmetry for perturbation fields (in magnitude) about the mountain center. Strong downslope winds are produced in the lee of the mountain with a corresponding region of strong turbulence. The intensity of the upper-level fields was weaker than predicted by linear theory. The total wave drag was found to increase faster than h^2, as predicted by linear theory. The calculations presented in this paper were mainly intended to demonstrate the model's capabilities. Far more extensive calculations and analyses must be performed before any firm conclusions can be arrived at with respect to the mountain wave drag problem. These are the subject of current investigation.

It was found that the total wave drag value is slightly sensitive to the start-up procedure. A smooth start-up allowed for a converged wave drag value with respect to increasing lateral extent. This sensitivity is attributed to the upstream propagation of transient waves, which is reflected by the free slip inflow boundary condition, i.e., the free slip on the perturbation field components. Future calculation of wave drag cases with this model will certainly require either a smooth start-up scheme and/or the inclusion of an upstream radiation boundary condition similar to that used at the outflow.

REFERENCES

1. G. K. BATCHELOR, *Quart. J. Roy. Meteorol. Soc.* **29** (1953), 224.
2. Y. OGURA AND J. G. CHARNEY, *in* "Proceedings of the International Symposium on Numerical Weather Prediction, Tokyo, 1960," pp. 431–452, Meteorol. Soc., Tokyo.
3. Y. OGURA AND N. A. PHILLIPS, *J. Atmos. Sci.* **19** (1962), 173.
4. I. VERGEINER, *Quart. J. Roy. Meteorol. Soc.* **97** (1971), 30.
5. J. B. KLEMP AND D. K. LILLY, *J. Atmos. Sci.* **32** (1975), 320.
6. TZVI GAL-CHEN AND R. C. J. SOMERVILLE, *J. Computational Phys.* **17** (1975), 209.
7. TZVI GAL-CHEN AND R. C. J. SOMERVILLE, *J. Computational Phys.* **17** (1975), 276.

8. A. J. CHORIN, *Math. Comp.* **22** (1968), 745.
9. A. ARAKAWA, *J. Computational Phys.* **1** (1966), 119.
10. I. ORLANSKI, *J. Computational Phys.* **21** (1976), 251.
11. J. BOUSSINESQ, "Theoric analytique de la chaleur," Vol. 2, p. 9, Gauthier–Villars, Paris, 1903.
12. J. SMAGORINSKY, *Monthly Weather Review* **91** (1963), 99.
13. D. K. LILLY, *Tellus* **14** (1962), 148.
14. F. H. HARLOW AND J. E. WELCH, *Phys. Fluids* **8** (1965), 2182.
15. H. O. KREISS, *in* "Proceedings of a Symposium at the University of Wisconsin, May 1966" (D. Greenspan, Ed.) Wiley, New York, 1966.
16. I. ORLANSKI, personal communication.
17. M. OGURA, *J. Meteorol. Soc. Japan* **47** (1969), 324.
18. W. R. PELTIER, personal communication.
19. J. W. MILES AND H. E. HUPPERT, *J. Fluid Mech.* **35** (1969), 497.
20. P. QUENEY, "Theory of Perturbations in Stratified Currents with Applications to Air Flow over Mountains," Univ. of Chicago Press, Chicago, 1947.
21. F. SHUMAN, *in* "Proceedings of the International Symposium on Numerical Weather Prediction, Tokyo, 1960," p. 85, Meteorol. Soc., Tokyo.
22. J. M. GARY, *J. Atmos. Sci.* **30** (1973), 223.
23. A. LAPIDUS, *J. Computational Phys.* **2** (1967), 154.
24. J. L. ANDERSON, S. PREISER, AND E. L. RUBIN, *J. Computational Phys.* **2** (1968), 279.